



# Capturing a methanogenic carbon monoxide dehydrogenase/acetyl-CoA synthase complex via cryogenic electron microscopy

Alison Biester<sup>a</sup> , David A. Grahame<sup>b</sup> , and Catherine L. Drennan<sup>a,c,d,1</sup>

Affiliations are included on p. 10.

Edited by Janet Smith, University of Michigan–Ann Arbor, Ann Arbor, MI; received June 1, 2024; accepted August 27, 2024

Approximately two-thirds of the estimated one-billion metric tons of methane produced annually by methanogens is derived from the cleavage of acetate. Acetate is broken down by a Ni–Fe–S-containing A-cluster within the enzyme acetyl-CoA synthase (ACS) to carbon monoxide (CO) and a methyl group ( $\text{CH}_3^+$ ). The methyl group ultimately forms the greenhouse gas methane, whereas CO is converted to the greenhouse gas carbon dioxide ( $\text{CO}_2$ ) by a Ni–Fe–S-containing C-cluster within the enzyme carbon monoxide dehydrogenase (CODH). Although structures have been solved of CODH/ACS from acetogens, which use these enzymes to make acetate from  $\text{CO}_2$ , no structure of a CODH/ACS from a methanogen has been reported. In this work, we use cryo-electron microscopy to reveal the structure of a methanogenic CODH and CODH/ACS from *Methanoscincus thermophilus* (*Met*CODH/ACS). We find that the N-terminal domain of acetogenic ACS, which is missing in all methanogens, is replaced by a domain of CODH. This CODH domain provides a channel for CO to travel between the two catalytic Ni–Fe–S clusters. It generates the binding surface for ACS and creates a remarkably similar CO alcove above the A-cluster using residues from CODH rather than ACS. Comparison of our *Met*CODH/ACS structure with our *Met*CODH structure reveals a molecular mechanism to restrict gas flow from the CO channel when ACS departs, preventing CO escape into the cell. Overall, these long-awaited structures of a methanogenic CODH/ACS reveal striking functional similarities to their acetogenic counterparts despite a substantial difference in domain organization.

greenhouse gases | methanogenesis | gas channels | cryogenic electron microscopy

Acetogens and methanogens are theorized to be the first life forms because they are capable of autotrophic growth on  $\text{CO}_2$  and  $\text{H}_2$ , gases thought to be abundant in the early atmosphere (1, 2). These microbes can synthesize acetate, a basic building block of life, from two molecules of  $\text{CO}_2$  with reducing equivalents derived from  $\text{H}_2$ . A key enzyme involved is a 310 kDa bifunctional carbon monoxide dehydrogenase (CODH)/acetyl-CoA synthase (ACS), which utilizes multimetal ion cofactors composed of nickel, iron, and sulfur (3). Conservation in both bacterial and archaeal domains of life suggests that CODH and ACS are among the oldest enzymes and were present in the last universal common ancestor (LUCA) (1, 4). In the modern global carbon cycle, acetogens and methanogens contribute approximately  $10^9$  tons of acetate and  $10^9$  tons of methane, respectively, each year (5, 6).

CODH of acetogenic CODH/ACS uses a Ni–Fe–S-containing C-cluster to reversibly reduce  $\text{CO}_2$  to CO, the biological equivalent of the water-gas shift reaction (Scheme 1 and *SI Appendix*, Fig. S1A). The generated CO travels through a gas channel (7, 8) within CODH/ACS to the Ni–Fe–S-containing A-cluster of ACS where it is combined with a methyl moiety and coenzyme A to make acetyl-CoA, in the biological equivalent of the Monsanto process (Scheme 1 and *SI Appendix*, Fig. S1A). In acetogens, the methyl group is delivered to the A-cluster by an 83 kDa corrinoid iron-sulfur protein (CFeSP), using its Co-containing corrinoid cofactor (Scheme 1 and *SI Appendix*, Fig. S1A and D). Thus, acetyl-CoA production requires both a bifunctional CODH/ACS and a standalone CFeSP (9, 10). By contrast, methanogenic archaea employ four copies of CODH ( $\alpha_2\epsilon_2$  heterotetramers) and eight copies of ACS ( $\beta$  monomers) that interact stably with eight copies of CFeSP ( $\gamma\delta$  heterodimers) to form a massive 2.2 MDa complex called the acetyl-CoA decarbonylase/synthase (ACDS) complex (*SI Appendix*, Fig. S1B) (11–13). Approximately two-thirds of the estimated one-billion metric tons of methane produced annually by methanogens on Earth is derived from the cleavage of acetate (5, 14, 15). ACDS plays a central role in that process, wherein the A-cluster of ACS cleaves acetyl-CoA into CO and a methyl moiety, the C-cluster of CODH oxidizes CO to  $\text{CO}_2$ , and the corrinoid of

## Significance

Carbon monoxide dehydrogenase (CODH) and acetyl-CoA synthase (ACS) play major roles in the global carbon cycle through the consumption of CO and  $\text{CO}_2$  gases, production of acetate, and breakdown of acetate for methane generation. These enzymes are proposed to have been present in the last universal common ancestor based on sequence conservation of CODH and ACS between bacterial and archaeal domains of life. To complement published structural studies of bacterial CODH/ACS complexes, here we present the structure of an archaeal CODH/ACS complex and discuss intriguing similarities between bacterial and archaeal CODH/ACS enzymes. This work provides insights into the common features of CODH/ACS that were likely present in the enzymes utilized by Earth's earliest life forms.

Author contributions: A.B., D.A.G., and C.L.D. designed research; A.B. and D.A.G. performed research; A.B., D.A.G., and C.L.D. analyzed data; and A.B., D.A.G., and C.L.D. wrote the paper.

The authors declare no competing interest.

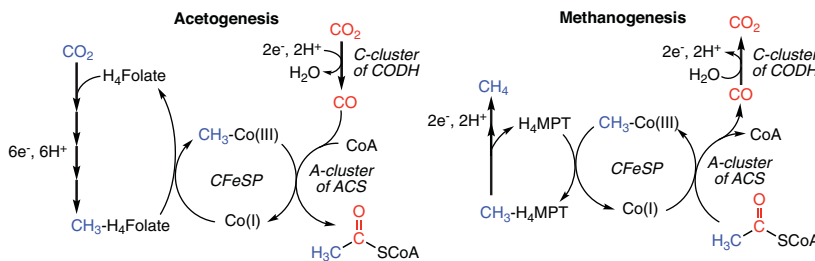
This article is a PNAS Direct Submission.

Copyright © 2024 the Author(s). Published by PNAS. This open access article is distributed under [Creative Commons Attribution License 4.0 \(CC BY\)](#).

<sup>1</sup>To whom correspondence may be addressed. Email: cdrennan@mit.edu.

This article contains supporting information online at <https://www.pnas.org/lookup/suppl/doi:10.1073/pnas.2410995121/-DCSupplemental>.

Published October 3, 2024.



**Scheme 1.** Pathways of acetogenesis and methanogenesis.

CFeSP receives the methyl moiety, which is reduced to methane in downstream methanogenic metabolism (Scheme 1 and *SI Appendix*, Fig. S1B). However, archaea can also use ACDS for acetyl-CoA synthesis, which was likely the way ACDS was used in early archaeal metabolism (16, 17). Finally, in the absence of ACS, CODH can couple CO oxidation to hydrogen production (*SI Appendix*, Fig. S1C) (18). Such monofunctional CODHs are believed to have originated early in bacterial evolution by gene duplication from the CODH of a bifunctional CODH/ACS complex (4). These enzymes are estimated to eliminate approximately  $10^8$  tons of CO from the atmosphere annually (19).

Monofunctional CODHs were the first to be structurally characterized (20, 21). They were found to be homodimeric, where each monomer consists of an N-terminal helical domain and two Rossmann folds (*SI Appendix*, Fig. S2A). Each homodimer contains five metalloclusters (*SI Appendix*, Fig. S1D), including one 4Fe–4S B-cluster per monomer and one 2Fe–2S or 4Fe–4S D-cluster bridging the monomers, all of which are bound by the N-terminal helical domain (20–24). The D- and B-clusters are responsible for transferring electrons to and from the catalytic Ni–Fe–S C-cluster, which is sandwiched between the two Rossmann folds in each monomer.

The structure of a bifunctional CODH/ACS heterotetramer from the acetogen *Moorella thermoacetica* (*Moor*) (25) revealed the use of N- and C-terminal extensions from a classic CODH core fold to bind ACS, which has a three-domain structure (*SI Appendix*, Fig. S2B and C). The N-terminal domain of ACS, termed A1, is composed of a helical bundle preceding a Rossmann fold. The central domain and C-terminal domains, termed A2 and A3, respectively, are both  $\alpha/\beta$  domains. The A3 domain binds the catalytic Ni–Fe–S A-cluster. More recently, another acetogenic CODH/ACS from *Clostridium autoethanogenum* (*Ca*) was structurally characterized, revealing an enzyme with the same overall fold, but a dramatically different interface between CODH and ACS (*SI Appendix*, Fig. S2C) (26). The *Ca*CODH does not contain the N- and C-terminal extensions found in *Moor*CODH, and instead binds ACS through a loop and helix at the N-terminal end of Rossmann fold 2 (helix  $\alpha$ A and preceding loop, *SI Appendix*, Fig. S2A and C). In both *Ca* and *Moor*CODH/ACS, it is the A1 domain of ACS used to bind CODH (*SI Appendix*, Fig. S2B and C).

Much less is known about the structures of the methanogenic ACDS proteins, the focus of this study. Only one component, the methanogenic CODH heterotetramer as isolated from an ACDS complex, has been structurally characterized (*SI Appendix*, Fig. S3A) (27, 28). The N-terminal helical domain, Rossmann folds 1 and 2, and the B-, C-, and D-clusters of the monofunctional and acetogenic CODH are also present in the methanogenic CODH from *Methanosarcina barkeri* (*Meb*); however, the methanogenic CODH has several key differences in its fold and has additional chains, domains, and cofactors. The additional chain in methanogenic CODH is called the  $\epsilon$  subunit, in which a single Rossmann fold is the major structural element; this chain binds the  $\alpha$  subunit and buries the D-cluster. Between the two Rossmann

folds of the  $\alpha$  subunit, there is an iron-sulfur cluster domain insert harboring two additional 4Fe–4S clusters, the E- and F-clusters; the F-cluster is surface exposed and acts as the entry point for transferring electrons to and from the C-cluster active site. Finally, the  $\alpha$  subunit of the methanogenic CODH contains a C-terminal extension. From sequence information we know that this ACS lacks the A1 domain but has A2 and A3 domains conserved with its monofunctional and acetogenic ACS counterparts, along with a unique C-terminal extension (*SI Appendix*, Fig. S3B).

The absence of the A1 domain in methanogenic ACS raises several questions. First, in acetogens, A1 serves as the binding domain for CODH, so it is unclear how ACS binds to CODH in methanogens. Second, the gas channel that carries CO from the C-cluster in CODH to the A-cluster in acetogenic CODH/ACSSs (*SI Appendix*, Fig. S4A) is a major component contained in the A1 domain, which raises the question of how CO transits between the clusters in methanogens (28). Third, A1 of *Moor*CODH/ACS contributes residues to the upper face of the A-cluster, forming an alcove for a cluster-bound CO molecule when the gas channel is open (*SI Appendix*, Fig. S4A, inset) (29, 30). Whether or not a similar CO alcove exists in methanogen ACS, and how similar or different it might be, has been a subject of speculation and motivation for structural studies.

Important protein conformational changes are implicated in the CODH/ACS mechanism. *Moor*ACS must open up to expose the otherwise buried A-cluster to allow for methylation by CFeSP. Evidence for this movement has been obtained from both crystallography (29, 31) and by negative stain EM (32), which involves swinging of A2 and/or A3 away from A1 (*SI Appendix*, Fig. S4B), and also, the closing of the gas channel by movement of helix  $\alpha$ A of A1 (*SI Appendix*, Fig. S4B, inset) (31). Thus, at least two different major conformations exist for *Moor*CODH/ACS, an open-channel/closed ACS for A-cluster carbonylation and a closed-channel/open ACS for A-cluster methylation. For both states, the A1 domain of ACS plays a key role, but how these dynamic changes are accomplished in methanogens in the absence of A1 is entirely unknown.

In this study, we investigate the structure of methanogenic CODH and CODH/ACS complexes from *Methanosaicina thermophila* (*Met*). Through plunge freezing of the ACDS complex, we captured multiple subcomplexes including a CODH tetramer, a CODH/ACS pentamer, and a CODH/ACS hexamer and characterized these subcomplexes via cryogenic electron microscopy (cryo-EM). These structures reveal a CODH/ACS interface that differs from the interface observed in acetogens but displays a remarkably similar CO-binding alcove. We observe a hydrophobic cavity between the C- and A-clusters in the CODH/ACS complex that is likely used for gas transport, and notably is much shorter than the channel in *Moor*CODH/ACS. In comparing the CODH alone with the CODH/ACS complex, we have identified a molecular mechanism to close the gas channel when ACS is absent. This molecular mechanism is like that of *Moor*CODH/ACS. The results contribute a substantial advance to the understanding of key

structural and functional similarities and differences between the acetogenic and methanogenic CODH/ACS interactions.

## Results

**Sample Preparation on Next-generation Automated Chameleon Plunging Instrument Yields CODH/ACS Subcomplexes.** Previous work on the methanogenic ACDS complex has shown that subcomponents can be isolated using treatments with detergent or limited proteolysis, along with ion exchange chromatography (33–35). Through these methods, the  $\alpha_2\epsilon_2$  CODH subunit (33–35), a truncated form of the  $\beta$  ACS subunit (33, 34), and the  $\gamma\delta$  CFeSP subunit (30) have each been isolated, as well as a  $\beta(\gamma\delta)$  ACS/CFeSP subcomplex (34). However, isolation and characterization of an  $(\alpha_2\epsilon_2)\beta$  CODH/ACS subcomplex has not been reported. In this work, all experiments were performed using intact *MetACDS* complex, and on-grid dissociation allowed for visualization of subcomponents through cryo-EM. Using a traditional blot-plunging method,  $\alpha_2\epsilon_2$  CODH subcomplexes were observed (Fig. 1A and *SI Appendix*, Table S1). Sufficient CODH subcomplex was present on the grid to generate a high-resolution reconstruction, however, in 2D and 3D classifications of CODH particles, there were no classes containing additional density consistent with ACS (*SI Appendix*, Figs. S5 and S6). With the next-generation chameleon instrument (36, 37), different dissociation behavior led to formation of  $(\alpha_2\epsilon_2)\beta$  and  $(\alpha_2\epsilon_2)\beta_2$  CODH/ACS subcomplexes in addition to the  $\alpha_2\epsilon_2$  CODH subcomplexes, allowing us to capture methanogenic CODH/ACS subcomplexes (Fig. 1B and *SI Appendix*, Figs. S7–S9 and Table S1). The chameleon technology, based on Spotiton (38, 39), is intended to ameliorate issues of particle denaturation, and it is therefore unsurprising that we observe differences in dissociation behavior relative to the blot-plunge method. Findings using the

chameleon instrument have demonstrated that short dispense-to-plunge times (<300 ms) can help mitigate particle denaturation (40, 41), and another study showed that the chameleon can yield transient protein oligomeric states in sufficient abundance for structure determination, which was not true when using blot-plunging (42). Here, we observe a similar phenomenon, wherein the full 2.2 MDa ACDS complex is dissociated to a lesser extent on the chameleon than on a blot-plunger; in both the blot-plunged specimen and the chameleon-plunged specimen, CODH particles were observed, but CODH/ACS subcomplexes were only observed in the chameleon-plunged specimen, suggesting that the ACDS complex underwent more dissociation under blot-plunging conditions. The use of two plunging methods allowed us to capture two snapshots of *MetCODH*, with global resolutions of 2.8 and 3.3 Å for the maps from chameleon and Cp3-plunged samples, respectively (Fig. 1A and B and *SI Appendix*, Figs. S6 and S10). Additionally, from the chameleon-plunged specimen, structures of the *MetCODH/ACS* pentamer and hexamer were determined, each at a global resolution of 3.2 Å (Fig. 1B and *SI Appendix*, Figs. S11 and S12).

**Unique CODH/ACS Interface Is Observed in Methanogens.** The *MetCODH*  $\alpha_2\epsilon_2$  heterotetramer shares the same topology as *MebCODH* (Fig. 2 and *SI Appendix*, Figs. S3A and S13A) and harbors the same set of metallocofactors, including E- and F-clusters, which are not present in monofunctional and acetogenic CODHs (*SI Appendix*, Figs. S13 B and C and S14 B–F) (28). As expected based on the amino acid sequence (43, 44), *MetACS* shares the topology as the A2 and A3 domains of monofunctional and acetogenic ACSs, but lacks the N-terminal A1 domain (Fig. 2 and *SI Appendix*, Figs. S2B, S3B, and S13A). Although *MetACS* contains an ~75 amino acid C-terminal extension of unknown function, that extension could not be resolved in our EM data and is likely highly

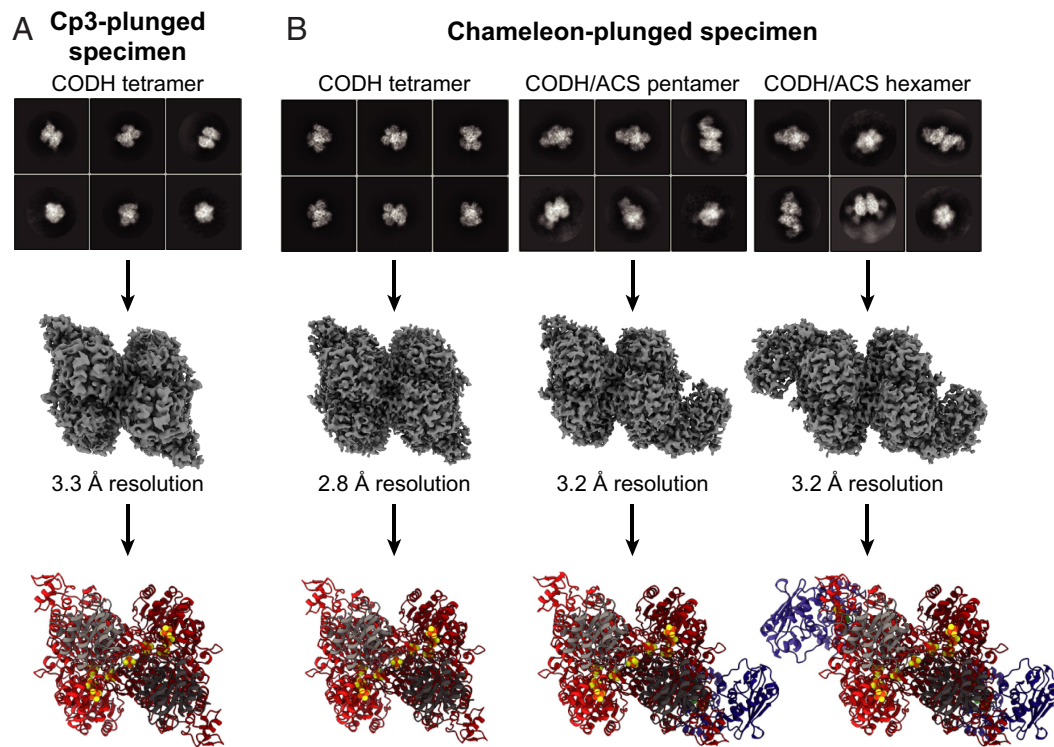


**Fig. 1.** Traditional EM grid blot-plunging yields CODH tetramer particles, whereas chameleon-plunging yields CODH tetramer, CODH/ACS pentamer, and CODH hexamer subcomplexes. (A) 2D classes, final EM map, and model of CODH tetramer particles from Cp3-plunged specimen. (B) 2D classes, final EM maps, and models of CODH tetramer, CODH/ACS pentamer, and CODH/ACS hexamer from chameleon-plunged specimen. CODH  $\alpha$  subunits are colored in red, CODH  $\epsilon$  subunits are colored in gray, and ACS  $\beta$  subunits are colored in blue.

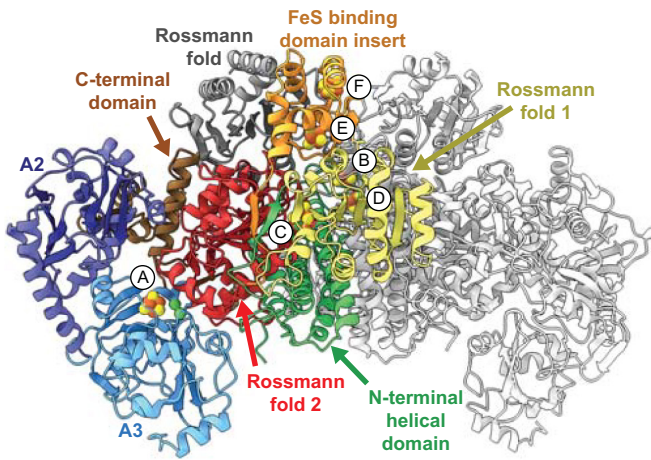


**Fig. 2.** CODH/ACS hexameric complex from *M. thermophila*. The locations of domains and cofactors are indicated.

flexible. To facilitate comparisons with its acetogenic counterparts, the two ACS domains of *M. thermophila* are referred to here as the A2 (central domain, residues 4 to 151) and A3 (C-terminal domain, residues 186 to 397).

The structures reported here reveal that both A2 and A3 of ACS contact CODH (Fig. 2). This interface does not bear resemblance to any previously observed CODH/ACS interface; all reported CODH/ACS structures to date are from acetogenic bacteria, wherein it is solely A1 of ACS that interacts with CODH (*SI Appendix*, Fig. S13A). On CODH, the interaction surface is formed largely by Rossmann fold 2 (Fig. 2). Interestingly, the C-terminal extension of *MetCODH*, which differs from the C terminus of non-methanogenic CODHs, interacts with ACS. The *MetCODH*/ACS interface is also distinct because this interaction includes direct packing of the A-cluster against CODH.

**CO-Binding Alcove in Acetogens Is Conserved in Methanogens.** In the structure of *MetCODH*/ACS, we observe density consistent with CO binding to the proximal nickel of the A-cluster (*SI Appendix*, Fig. S14A). The geometry of Ni<sub>p</sub> is tetrahedral as observed previously for a CO-bound A-cluster (29). Superimposition with the CO-bound *MoorCODH*/ACS structure (aligned with respect to A3 of ACS) reveals several similarities despite the interface differences. Where in *MoorACS*

A1 packs against A3, in *MetCODH*/ACS we find Rossmann fold 2 of CODH packed against A3 of ACS in an analogous fashion, and the helices preceding the Rossmann fold of *MoorACS* align with the N-terminal helical domain of *MetCODH* (Fig. 3A and *SI Appendix*, Fig. S13 D and E). The environment surrounding the CO-bound A-cluster of *MetCODH*/ACS is remarkably similar to that of *MoorCODH*/ACS. In *MoorCODH*/ACS, four second-sphere residues have been noted as important for forming the CO-binding alcove: Ile146 and Val149 on helix αA and Phe229 on helix αB from A1, and Phe512 from A3 (29, 30). Phe512 of *MoorACS* is conserved in the A3 domain, corresponding to Phe195 in *MetACS* (Fig. 3B and *SI Appendix*, Figs. S15 and S16A). Substituting for Ile146, Val149, and Phe229 of the A1 domain of *MoorACS* are Leu504, Val507, and Phe601 of Rossmann fold 2 in *MetCODH*, respectively (Fig. 3B and *SI Appendix*, Figs. S15 and S16B). An interaction made to an A-cluster coordinating residue is also conserved. Arg142 of the A1 domain of *MoorACS* corresponds to Arg500 of Rossmann fold 2 in *MetCODH*. Both arginine residues hydrogen bond with the carbonyl of a glycine whose backbone nitrogen coordinates Ni<sub>d</sub> (Fig. 3C).

**The CO Channel for Methanogenic CODH/ACS Is Also Observed in Monofunctional CODH but Differs From Paths in Acetogenic CODH/ACSS.** Xenon gas has been used to map gas channels in the monofunctional CODH from *Desulfovibrio vulgaris* (45). Two channels were identified, with channel 1 traversing from near the C-cluster to the enzyme surface, whereas channel 2 branches off into channels 2A and 2B, with each branch leading to the enzyme surface (Fig. 4A and *SI Appendix*, Fig. S17A). Channel 1 from the monofunctional CODH aligns with the C- to A-cluster gas channel in *MoorCODH*/ACS (Fig. 4B and *SI Appendix*, Fig. S17B) as elucidated via xenon gassing studies (46) and observed in cavity calculations. Structural analysis shows that the distance between the C- and A-cluster in *MoorCODH*/ACS is ~70 Å, with the cavity between them weaving through the protein along a path that totals ~110 Å in length, based on cavity calculations. For *CaCODH*/ACS, which displays a different ACS:CODH interface (26), the gas channel is rerouted relative to the *Moor* enzyme (based on cavity calculations). The channel in *CaCODH* is shared with channels 2 and 2A in the monofunctional CODH (Fig. 4C and *SI Appendix*, Fig. S17C). Upon performing cavity calculations on the *MetCODH*/ACS complex, we see that this enzyme uses channel 2, like *CaCODH*/ACS, but *MetCODH*/ACS uses the channel 2B branch (Fig. 4D and *SI Appendix*, Fig. S17D). Given

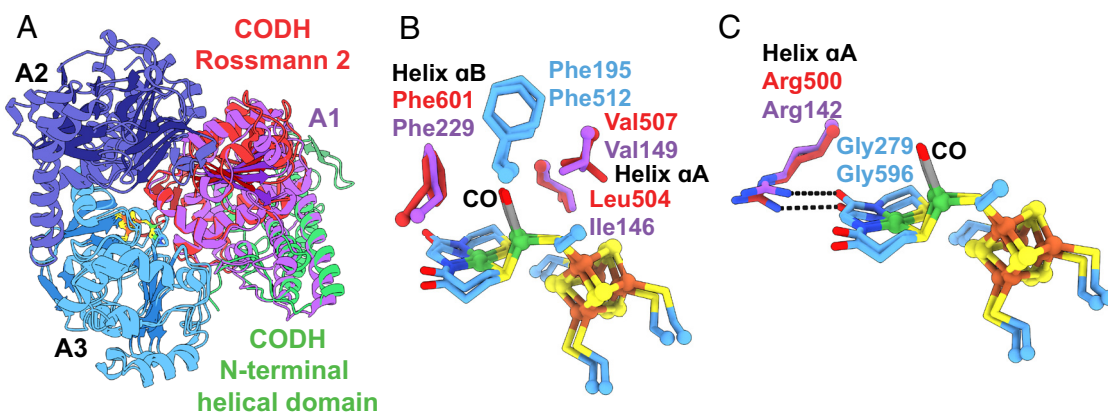


**Fig. 3.** *MetCODH* Rossmann fold 2 takes the place of *MoorACS* domain 1 and creates a CO alcove above Ni<sub>p</sub> in the A-cluster. (A) Overlay of *MetCODH* (red and green)/ACS (cyan and blue) with the closed conformation of *MoorACS* (PDBID: 6X5K) (A1 in purple). For clarity, only Rossmann fold 2 (red) and the N-terminal helical domain (green) of *MetCODH* are shown. (B) Conservation of residues in the CO alcove of the A-cluster between *MetCODH*/ACS and *MoorACS*. (C) Conservation of arginine: A-cluster interactions. The A-cluster is colored: Ni green; Fe orange; S yellow; CO gray/red. Carbons are colored by domains as in Fig. 2.

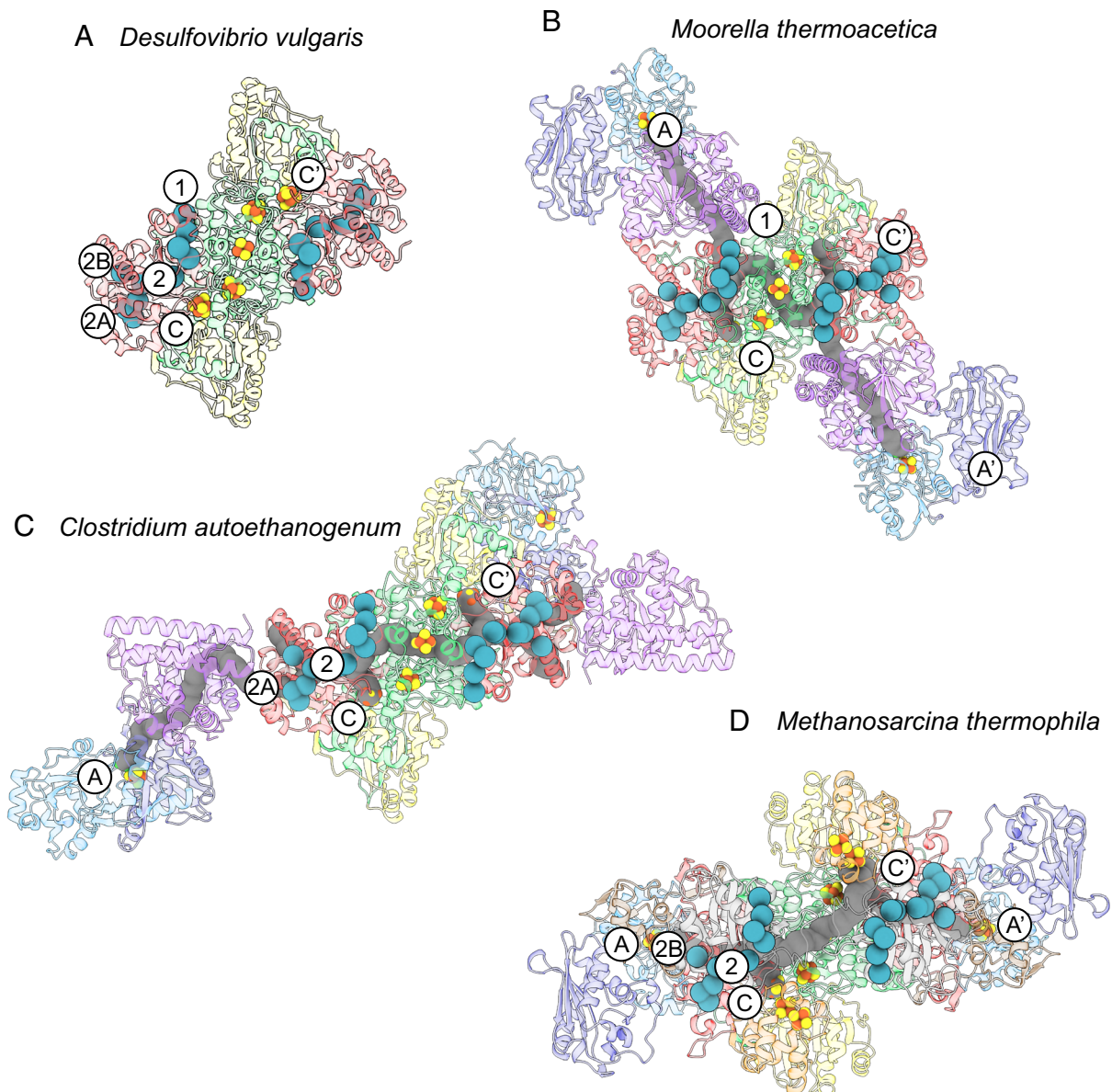


**Fig. 4.** Gas channels from monofunctional CODH compared with acetogenic and methanogenic CODH channels. (A) The monofunctional CODH from *D. vulgaris* has three gas channels (1, 2A, and 2B) elucidated by xenon studies (PDBID: 7TSJ). (B) Structure of *M. thermoacetica* CODH/ACS (PDBID: 6X5K) with calculated cavities. Xe sites from *D. vulgaris* CODH are overlaid. Channel 1, which is extended to form the CO gas channel spanning from the C- to A-cluster for the acetogenic CODH/ACS from *M. thermoacetica*. The C- and A-clusters, which are ~70 Å apart in *M. thermoacetica*, are connected by a channel that is ~110 Å long. (C) Structure of *C. autoethanogenum* CODH/ACS (PDBID: 6YTT) with calculated cavities. Xe sites from *D. vulgaris* CODH are superimposed. Channels 2 and 2A align with the CO gas channel leading from the C-cluster to ACS in the acetogenic CODH/ACS from *C. autoethanogenum*. (D) Structure of *M. thermophila* CODH/ACS (this work) with calculated cavities. Xe sites from *D. vulgaris* CODH are overlaid. Channels 2 and 2B align with the CO gas channel leading from the C- to A-cluster for the methanogenic CODH/ACS from *M. thermophila*. The C- and A-clusters in *M. thermophila*, which are ~35 Å apart, are connected by a channel that is ~50 Å long. Xe sites are shown as cyan spheres. Cavities were calculated using MOLEonline, and calculated cavities are shown in gray. Proteins are colored as in Fig. 2. See *SI Appendix*, Fig. S17 for calculated cavities without Xe sites superimposed.

that *MetACS* lacks A1, the ACS packs in more tightly to the CODH compared to the acetogenic CODH/ACS complexes, giving rise to a much shorter distance between the C- and A-clusters, with a measured distance of ~35 Å, and the internal cavity totaling ~50 Å in length. It is intriguing that all three channels observed in the monofunctional CODH are present in the distinct CODH/ACSS whose structures have been determined to date.

**Conformational Changes in CODH Facilitate Opening and Closing of the CO Channel.** In our structure of *MetCODH/ACS*, the channel between the C-cluster and A-cluster is open and resembles the open channel near the A-cluster in *MoorCODH/ACS* (Fig. 5). In both cases, the channel runs between two helices (labeled  $\alpha$ A and

$\alpha$ B in *SI Appendix*, Figs. S2B and S3A) and terminates in the CO-binding alcove (Fig. 5 and *SI Appendix*, Fig. S18). In the structures of *MetCODH* without ACS bound (Fig. 1), this CO channel is closed. The structural basis for channel closing appears similar to that previously observed for *MoorCODH/ACS* (31). In both cases, helix  $\alpha$ A shifts toward helix  $\alpha$ B to close the gas channel and block CO release. Instead of Val507(*Met*)/Val149(*Moor*), Leu504(*Met*)/Ile146(*Moor*), and Phe601(*Met*)/Phe229(*Moor*) creating an alcove for bound-CO (Fig. 4 and *SI Appendix*, Fig. S15), these residues now create a choke point in the CO channel (Fig. 5 and *SI Appendix*, Figs. S18 and S19). Additionally, helix  $\alpha$ A residue Arg500(*Met*)/Arg142(*Moor*) has repositioned so that it no longer hydrogen bonds to the A-cluster coordinating Gly279(*Met*)/Gly596(*Moor*) (Fig. 5

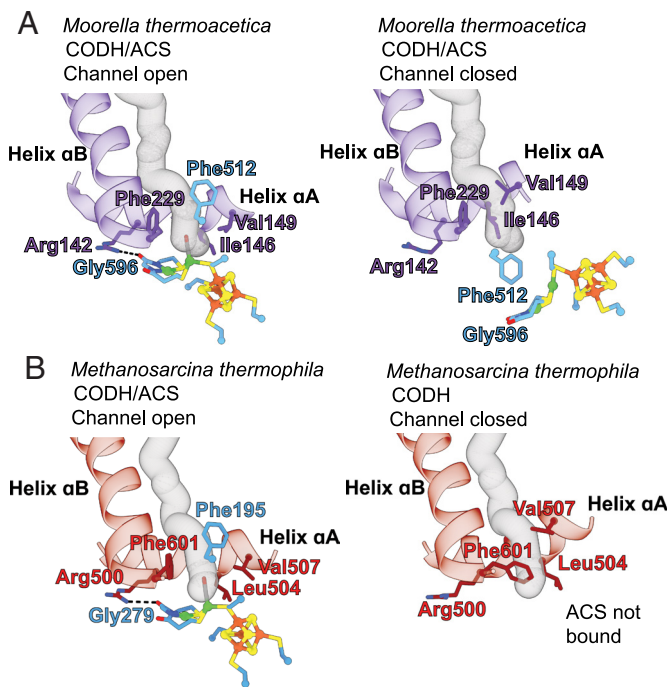


**Fig. 5.** Movement of conserved Rossmann helices caps the gas channel in acetogens and methanogens. (A) In the open-channel/closed-ACS conformation of *MoorACS* (PDBID: 6X5K), the gas channel passes between helices  $\alpha$ A and  $\alpha$ B, with alcove residues surrounding the CO site and Arg142 hydrogen bonding to an A-cluster coordinating residue (Gly596). In the closed-channel/open-ACS conformation of *MoorACS* (PDBID: 1OAO), helix  $\alpha$ A blocks the gas channel, Phe512 blocks the CO-binding site at the A-cluster, and Arg142 has swung away from the A-cluster breaking its hydrogen bond. (B) In *MetCODH/ACS*, the gas channel also passes between helices  $\alpha$ A and  $\alpha$ B, with alcove residues surrounding the CO site and Arg500 hydrogen bonding to an A-cluster coordinating residue (Gly279). In *MetCODH* (ACS not bound), helix  $\alpha$ A shifts to block the gas channel, with Phe601 also swinging in to block the channel.

and *SI Appendix*, Figs. S18 and S19). This type of protein motion in CODH is quite interesting, as conformational motion is not preceded in CODHs. Typically, ACS is known to be the highly dynamic protein in the CODH/ACS system, but here, Rossmann fold 2 of CODH takes the place of A1 of ACS, and as such also takes on a similar conformational change. Prior to this work, relatively little was known about gas channels in methanogenic ACDS complexes (28, 47). Now we see that methanogenic CODH/ACDSs do have a channel connecting their C- and A-clusters and that the channel can open and close using a similar mechanism to that observed in acetogenic CODH/ACDSs. In both cases, channel closing prevents CO release during the time that ACS domains reposition to interact with CFeSP for methyl transfer.

## Discussion

There are at least six known pathways for  $\text{CO}_2$  fixation (48, 49). The majority involve adding a molecule of  $\text{CO}_2$  to an already formed carbon chain. The chemistry catalyzed at the A-cluster is distinctive in that it creates a two-carbon chain from two one-carbon units. This carbon fixation ability is one of several reasons that A-cluster chemistry is believed to be ancient, perhaps predating protein synthesis with slurries of nickel, iron, and sulfur creating carbon chains (1). When the first structure of an acetogenic CODH/ACS was reported two decades ago (25), the role(s) of the protein in acetyl-CoA synthesis emerged. Although the Ni–Fe–S cluster is the catalyst that joins CO with  $\text{CH}_3$ , the protein controls CO access to the A-cluster via a gas channel that can open and close, and the protein controls  $\text{CH}_3$  group access via ACS domains that open and close. The protein can also sequester and stabilize

A-cluster reaction intermediates and tune redox potentials. Notably, the acetogenic CODH/ACS structure showed that it was the non-conserved A1 of ACS that seemed most critical for these functions, raising questions as to whether the CODH/ACS component of ACDS would function in an entirely different way and whether the role of protein in A-cluster chemistry is in fact conserved.

Twenty years after the first structure of a CODH/ACS, we now know that the role of the protein in the A-cluster-catalyzed acetyl-CoA synthesis is functionally conserved and that this conservation includes the housing of gas channels. As observed previously in acetogens (46), we find that the methanogenic protein also has a channel between its C- and A-clusters that plays a role of CO gatekeeper. Interestingly, the channel is present in monofunctional *DvCODH* but is not the one that is used by either acetogenic *Moor* or *CaCODH* (26, 45, 46). Monofunctional CODHs have three pathways that have been identified by xenon studies that extend from the C-cluster to the surface of CODH: channel 1, 2A, and 2B (Fig. 4) (45). We now have structures of three different CODH/ACDSs, two from acetogens and one from a methanogen, as reported in this work. In these complexes, each CODH binds ACS in a different way, and each CODH/ACDS complex utilizes a different gas channel as a result. Previous studies have described how amino acid substitutions in CODH/ACDSs are likely to close off channels to direct CO to that enzyme's A-cluster (45). The fact that we now see 3 of 3 xenon-identified routes employed in a CODH/ACDS raises the question as to whether we have now observed all the various ways in which an ACS can bind to a CODH.

Notably, the channel in methanogenic CODH/ACS is much shorter than it is in either of the structurally characterized acetogenic enzyme complexes. The longer channel in the acetogenic systems is created by the presence of the A1 domain, which extends the gas channel into the ACS subunit. A longer channel could provide a storage chamber or “waiting room” for CO in the acetyl-CoA synthetic direction, in which a slow protein conformational change at the A-cluster occurs in between each CO consumption step. However, there is no experimental evidence that multiple CO molecules reside in the gas channel under turnover conditions. The observed difference in gas channel lengths can still be rationalized if only one CO molecule exists in the channel at a time. There are two options for a CO molecule in the gas channel: CO can either be consumed by oxidation at the C-cluster or consumed by acetyl-CoA synthesis at the A-cluster. The  $K_M$  for CO oxidation at the C-cluster is higher than the  $K_M$  for acetyl-CoA synthesis at the A-cluster. This  $K_M$  difference favors CO oxidation when CO concentrations are high and favors acetyl-CoA synthesis when CO concentrations are low. One CO molecule in a short channel has an effective concentration that is higher, which would favor CO oxidation. One CO molecule in a large channel has a lower effective concentration, which would favor acetyl-CoA synthesis. Thus, the addition of the A1 domain to acetogenic CODH/ACDSs could have been an adaptation to lower the effective concentration of CO, thereby favoring acetyl-CoA synthesis, and possibly avoiding a futile cycle in which the C-cluster consumes the CO that it produced.

It is interesting to speculate on the evolutionary history of the A1 domain. A comprehensive phylogenomic study of CODH/ACDSs that utilized over 6,400 archaeal and bacterial genomes, supports the presence of a CODH/ACS in the LUCA, but the precise nature of that CODH/ACS could not be predicted (4). The close structural homology between the Rossmann 2 domain of CODH and the A1 domain of bacterial ACSs suggests a gene duplication event (Fig. 3). It is possible that this gene duplication happened before archaea and bacteria split, and that the A1 domain was lost to archaeal ACSs early on, explaining the lack of

this domain in all modern archaeal ACSs. Alternatively, the LUCA CODH/ACS might not have had an A1 domain. The A1 domain could have been added later via gene duplication of CODH Rossmann domain 2, perhaps providing a selective advantage to CODH/ACSs that utilize CO<sub>2</sub> as an electron sink, forming CO en route to synthesizing acetyl-CoA. Such a selective advantage would explain why this domain is found only in acetogenic bacteria but not in methanogenic archaea.

Unexpectedly, we find that acetogenic and methanogenic CODH/ACSs share the same mechanism of closing the CO gas channel, i.e., movement of helix  $\alpha$ A toward helix  $\alpha$ B (Fig. 5). In acetogenic CODH/ACS, it is helix  $\alpha$ A of ACS domain A1 that moves, and in methanogenic CODH/ACS, it is helix  $\alpha$ A of CODH Rossmann 2 that moves. Despite this difference, the mechanism appears conserved. This conservation of the channel plugging mechanism suggests a functional importance for preventing escape of CO. For acetyl-CoA synthesis, the generation of CO at the C-cluster comes at a cost of two low-potential electrons. Retaining CO in the channel of an acetogenic CODH/ACS ensures that low-potential reducing equivalents are not wasted. The low-potential electrons generated from CO oxidation are also crucial for acetoclastic methanogens, as they are used to drive reduction of the acetyl-CoA-derived methyl group to methane (11). Escape of CO from the channel into the cell could additionally lead to unwanted binding of CO to other metal centers or release of CO from the cell. For animals harboring acetogens and methanogens in their intestinal tracts, release of CO could be toxic (50–52). Therefore, it would be disadvantageous to leave the gas channel open when ACS has rearranged to engage with CFeSP.

In addition to being a gatekeeper for CO, the protein directly facilitates the binding of CO, CH<sub>3</sub>, and/or COCH<sub>3</sub> to the correct coordination site(s) on the A-cluster for catalysis, stabilizing bound states with the correct geometry for catalysis, and protecting such states from unwanted side reactions. In acetogens, A1 of ACS is responsible for these roles, and in methanogens, it is Rossmann 2 of CODH. The conservation of amino acids involved in these interactions is remarkable (Fig. 3). As observed for acetogenic enzymes, we find that a CO channel directs CO molecules to bind to the proximal Ni of the A-cluster (Ni<sub>p</sub>), and that residues of an alcove ensure that Ni<sub>p</sub>-CO adopts tetrahedral geometry (29). This alcove, composed of Leu504, Val507, and Phe601 from *MetCODH* and Phe195 from *MetACS*, also appears large enough for an acetyl moiety to fit while maintaining tetrahedral geometry of Ni<sub>p</sub>. It was previously proposed that sequestration of the acetyl-bound A-cluster must be important to prevent hydrolysis, which would form acetate rather than the valuable metabolic intermediate acetyl-CoA (46). A protein alcove above Ni<sub>p</sub> could thus have multiple functions. The protein also must play a critical role in ensuring the correct electron distribution in the A-cluster for the various steps of catalysis, and we find conserved amino acid residues support similar interactions in both acetogens and methanogens. These interactions include an Arg residue (Arg500 in *Met*) that hydrogen bonds to A-cluster-coordinating residue Gly279.

Another key role for the protein in A-cluster chemistry is to alternatively position the A-cluster for carbonylation by CODH and for methylation by CFeSP. No structure of ACS bound to CFeSP exists, but the structures of CODH/ACSs, including the one reported herein, indicate that domains must move for the A-cluster to be exposed and bind CFeSP. With the available structural and biochemical data, we can think about the conformational rearrangements that must occur during acetyl-CoA cleavage in a methanogenic ACDS complex (Figs. 6 and 7). Starting with acetylation of the A-cluster, an acetyl-bound Ni<sub>p</sub> would be expected to disassemble into CO and a CH<sub>3</sub> with both moieties migrating to

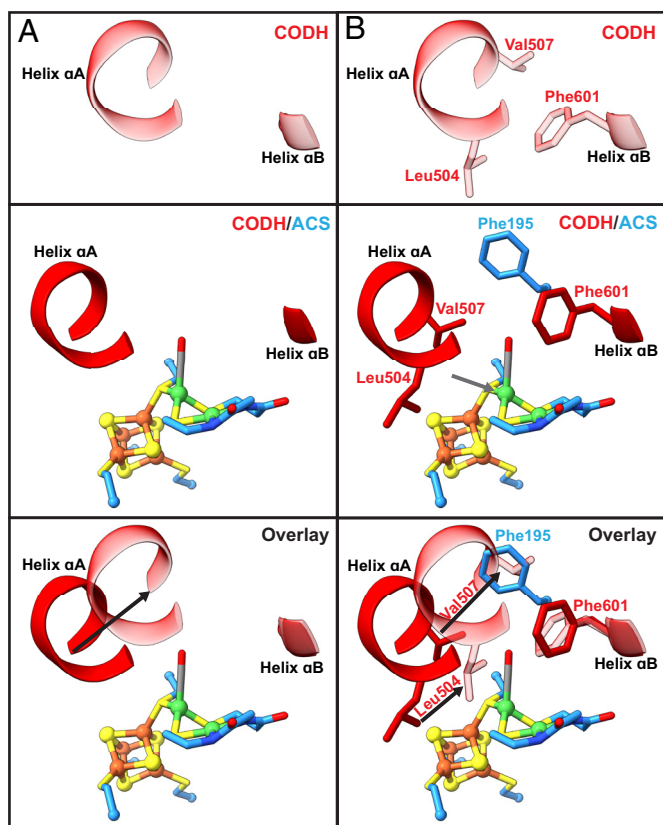


**Fig. 6.** Conformational change in *MetCODH* helix  $\alpha$ A and alcove residues should facilitate ACS departure from CODH. (A) Secondary structural movements in *MetCODH*. Top: Structure of *MetCODH* alone (transparent red). Middle: Structure of *MetCODH* (red)/ACS (blue). Bottom: Overlay of *MetCODH* (red)/ACS (blue) and *MetCODH* alone (transparent red) structures, showing a large shift in helix  $\alpha$ A. (B) Residue movements in *MetCODH*. Top: Structure of *MetCODH* alone, showing positions of alcove residues Leu504, Val507, and Phe601. Middle: Structure of *MetCODH* (red)/ACS (blue), showing the position of *MetCODH* alcove residues Leu504, Val507, Phe601, and *MetACS* residue Phe195. Bottom: Overlay of *MetCODH* (red)/ACS (blue) and *MetCODH* alone (transparent red) structures, showing movement of Leu504 toward Ni<sub>p</sub> and of Val507 toward Phe195. Black arrows are used to highlight helix and residue movements. The gray arrow in panel B indicates the putative methylation site on Ni<sub>p</sub>. For clarity, only residues discussed in the text are shown.

separate coordination sites on Ni<sub>p</sub> (Fig. 7, step 1). The CO should dissociate from Ni<sub>p</sub> via an open CO channel (Fig. 7, CODH/ACS<sub>Me</sub> open channel) and the resulting methyl-Ni<sub>p</sub> is expected to adopt square planar geometry based on X-ray absorption spectroscopy on *MoorACS* (53). Adoption of square planar geometry positions the methyl group out of the alcove. With the alcove empty, helix  $\alpha$ A is free to move toward helix  $\alpha$ B. The observed ~5-Å movement of helix  $\alpha$ A closes the channel but also should destabilize the ACS:CODH interface with CODH residue Val507 moving into the location occupied by alcove residue Phe195 of ACS and Leu504 moving close to the expected binding site for the methyl moiety on Ni<sub>p</sub> of the A-cluster (Fig. 6). A closed-channel state should therefore have weaker affinity for the methylated-A-cluster than the open-channel state, shifting the equilibrium toward ACS dissociation (Fig. 7, step 3). The correlation between the liganded state and geometry of Ni<sub>p</sub> with the state of the channel (open or closed) is also found in previous structural data; when Ni<sub>p</sub> adopts a tetrahedral geometry, the gas channel is open, whereas when Ni<sub>p</sub> adopts a square planar geometry, the gas channel is closed (*SI Appendix*, Table S2) (25, 29, 31, 54–56). Notably, interface analysis via PDBe PISA (57) shows that the number of contacts between *MetCODH* and *MetACS* is modest (*SI Appendix*, Tables S3–S5), meaning that the binding interaction should be very sensitive to changes in protein

structure and/or ligated state of the A-cluster. After ACS dissociates from CODH, ACS must associate with CFeSP for methyl transfer, forming the methylcorrinoid species (Fig. 7, step 4) (58, 59). The ACS/CFeSP complex then dissociates (Fig. 7, step 5) and ACS can reassociate with CODH (Fig. 7, step 6).

In the proposed reaction scheme for acetyl-CoA synthesis by *MetCODH*/ACS depicted in Fig. 7, methylation precedes carbonylation. The order of the reaction in *MoorCODH*/ACS has been debated in the literature (60) with arguments made for a random-order mechanism with either carbonylation first or methylation first (61), and also for an ordered mechanism with methylation first (62). A consensus has not yet been reached. In contrast, *MetCODH*/ACS has only been proposed to operate by a methylation-first mechanism based on extensive biochemical analyses (43, 47). In particular, the CO-bound A-cluster of *MetACS* has been shown to be an inhibited form of the A-cluster that cannot be methylated (43). This inhibition is reversible, and the A-cluster can lose CO and then be methylated (43). The structural data presented here provide a molecular explanation for both of these experimental observations. *MetACS* must dissociate from CODH to be methylated by CFeSP, and carbonylation of the A-cluster should decrease the tendency for CODH/ACS to dissociate because of the packing interactions made between CO and alcove residues thereby inhibiting methylation. Also, the structure suggests why CO inhibition is reversible: a CO molecule residing in the alcove can diffuse back into the gas channel, which would lead to helix  $\alpha$ A movement, prompting ACS departure. Once dissociated from CODH, *MetACS* would be free to interact with CFeSP for methylation. By disfavoring *MetACS* departure from CODH while the A-cluster is in the carbonylated state, the system protects against CO molecule loss that might occur while ACS is in transit.

To prevent formation of a CO-inhibited state, one can imagine that *MetCODH*/ACS has protein design features that limit the amount of carbonylation that can occur on an unmethylated

A-cluster, and those features do appear to be present. As described above, Leu504 of helix  $\alpha$ A is directly adjacent to the postulated methyl-coordination site on the A-cluster, and when the channel is closed, the distance would be unfavorably close (Fig. 6B). Such a close interaction would be expected to shift the conformational equilibrium of helix  $\alpha$ A toward the open-channel conformation, allowing for A-cluster carbonylation of a methylated A-cluster. By contrast, in the absence of a methyl ligand, ACS should still be able to bind to *MetCODH*, but without shifting the position of helix  $\alpha$ A, thereby maintaining a closed CO channel and limiting carbonylation and thus CO-inhibition of the A-cluster (43).

The structure obtained here of *MetCODH*/ACS likely relates to the previously described CO-inhibited state (43). It has not been possible to confirm the identity of the A-cluster ligand as CO via spectroscopy since we did not work with purified *MetCODH*/ACS but rather with purified ACDS that dissociated into multiple subcomplexes upon cryo-EM grid preparation (Fig. 1). Since ACDS was purified from the native organism while engaged in methanogenesis, the protein components likely represented a mixture of redox and liganded states. We hypothesize that when ACDS was isolated, some CO molecules remained in the channel. CO can be quickly consumed at the C-cluster, but only if the C-cluster oxidation state was proper, or if electron acceptors such as ferredoxin become unavailable (due to cellular disruption and dilution) this could result in residual, unconsumed CO within the gas channel. CO that remained in the channel would then have the option to return to bind at the A-cluster (after reassociation of ACS with CODH), and once bound, stabilize the CODH/ACS interaction due to favorable interactions in the CO-binding alcove, allowing us to visualize the complex on the EM grid. Although the increased stability afforded by a CO ligand in the alcove is substantial, it is unlikely large enough to allow for purification of the CODH/ACS subcomplexes by conventional methods. Accordingly, CODH/ACS

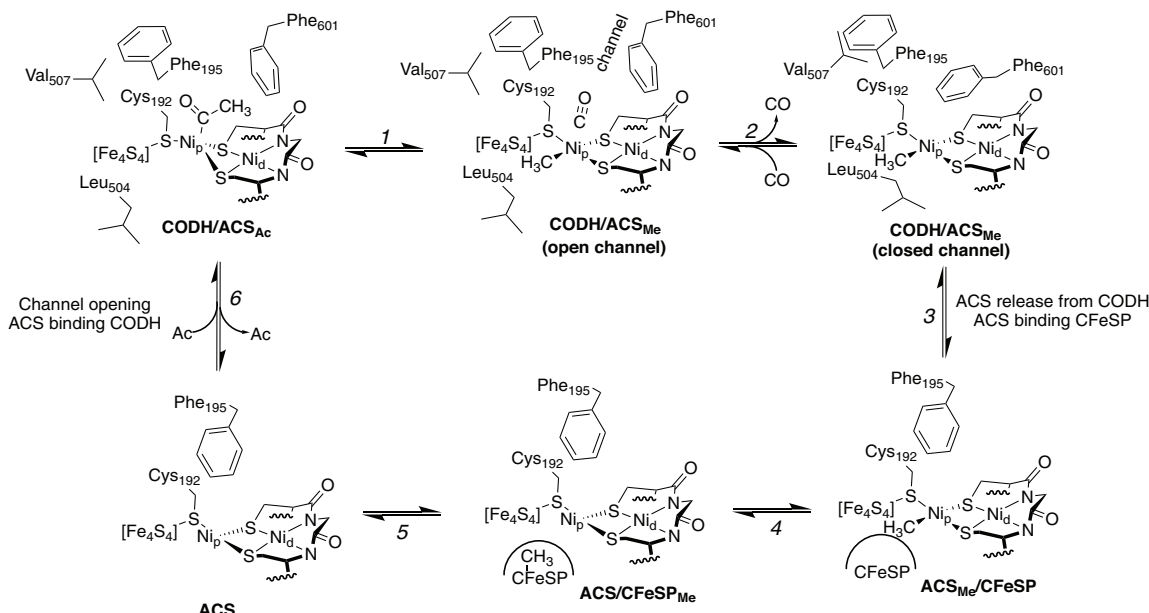


**Fig. 7.** Proposed protein conformational changes and resulting effects on the A-cluster environment in the mechanism of acetyl-CoA cleavage in ACDS. Steps are labeled 1 to 6. The proposed CODH/ACS<sub>Ac</sub> state is based on the geometry and residue positions of the CO-bound structure (this work, see Fig. 6B, Middle). Modeling suggests that an acetyl moiety can fit in the alcove but cannot fit in the predicted methyl coordination site due to the close positioning of Leu504. The geometry of the A-cluster shown for all ACS<sub>Me</sub> states is based on X-ray absorption spectroscopy on *MoorACS* (53). Residue positioning for CODH/ACS<sub>Me</sub> open-channel and closed-channel states is based on the observed residue positions (this work, Fig. 6B). The positioning of Phe195 when *MetACS* is not bound to *MetCODH* is based on the position of the analogous Phe512 in the closed-channel ACS structure of *MoorCODH*/ACS (Fig. 5A, Right) (31) and also on the loss of protection from CO inhibition when Phe195 of *MetACS* is substituted with Ala (43).

particles were only visualized in our chameleon-plunged specimen, which is considered a more rapid and gentler vitrification method. Even in our chameleon-plunged specimen, most of the observed CODH particles did not have ACS bound. In short, determination of this methanogenic CODH/ACS structure would not have been possible without the “resolution revolution of cryo-EM” (64) or without the improved particle picking and sorting software that allows for structures to be obtained from heterogeneous protein samples (65–68) or without the development of gentler blot-free plunging methods (36, 37, 39).

In conclusion, these structural studies have provided a long-awaited snapshot of a methanogenic CODH/ACS complex. However, the structural work is not complete. We are still lacking visualization of the interaction between ACS and CFeSP from any organism, which would provide much needed insight into the methyl transfer step of ACS catalysis. We are also missing structural data on the C-terminal extension of *MetACS* that is likely to play a role in the conformational rearrangements that ACS must make as it swings between CODH and CFeSP within the 2.2 MDa ACDS complex. Further study of the ACDS complex will be crucial for understanding the unique aspects of this system. Although the structures of acetogenic and methanogenic systems for acetyl-CoA synthesis and cleavage show marked differences, our work demonstrates that these systems have more in common than previously appreciated, including a conserved CO-binding alcove and channel gating mechanisms. These structural insights are likely to promote renewed discussion of the mechanism of the A-cluster of ACS, bringing us closer to a unified understanding of how nature makes acetyl-CoA from CO<sub>2</sub>-derived one-carbon units, and how it breaks acetyl-CoA into two one-carbon units en route to the production of greenhouse gases CO<sub>2</sub> and methane. Although this chemistry is ancient, it is no less relevant today as we seek novel ways to reduce the levels of greenhouse gases in our environment.

## Materials and Methods

**Growth of *M. thermophila*.** The method for growth of *Methanosarcina barkeri* on acetate (69) was modified for large-scale growth of *M. thermophila*, as described in detail (70). Briefly, *M. thermophila* strain TM-1 was grown at 50 °C in a minimal salts medium containing 2.5 g/L sodium acetate and 2.5 g/L potassium acetate trihydrate, supplemented with 0.15 g/L yeast extract. Anaerobic medium was reduced with 0.175 g/L cysteine-HCl monohydrate and 0.075 g/L sodium sulfide nonahydrate. Actively growing starter cultures were used for 1:10 inoculation of 20 L batch cultures. Glacial acetic acid was added during growth to maintain pH between 6.4 and 6.8. After gas production and acetic acid consumption reached a maximum, constant rate (~5 to 7 L gas evolved per hour) 50 to 70 h after inoculation, the cultures were chilled and then harvested anaerobically using a flow-through Sharples type centrifuge. Yield was 60 to 80 g cell paste per 20 L batch, which was frozen in liquid N<sub>2</sub> and stored in the vapor phase of a liquid N<sub>2</sub> storage unit.

**Purification of the ACDS Complex.** Preparation of soluble extracts from *M. thermophila* and isolation of the ACDS complex followed the same general approach as described for *M. barkeri* (11) except that the procedure was scaled down for use inside a Coy type anaerobic chamber. Briefly, frozen *M. thermophila* cell paste, 10 to 12 g, was thawed with addition of 30 mL of anaerobic Buffer A (50 mM MOPS-Na and 100 mM Na<sub>2</sub>SO<sub>4</sub>, pH 7.2) and disrupted by a single pass through a chilled 40-mL French press cell (1-inch diameter piston) at 18,000 to 20,000 psi. Following addition of DNase I to reduce the viscosity, the extract was centrifuged at ~48,000×g for 22 min at 0 to 4 °C, and the supernatant was collected. Additional discussion of the extraction procedure, including the techniques used to maintain anaerobic conditions throughout, can be found in ref. 70.

For purification of ACDS, the extract supernatant was applied to a column of Sepharose CL-6B (95 × 2.6 cm diameter) equilibrated in anaerobic Buffer A at a rate of 0.75 mL/min. Fractions were collected at 10 min intervals and assayed for protein (Bradford reagent, BioRad) (71) and CO dehydrogenase activity (in reaction mixtures containing 10 mM methylviologen and 0.1 M Tris-HCl, pH 8.0,

saturated with 100% CO at 25 °C). The ACDS complex eluted as a brown, high-molecular-weight protein peak that emerged from the column after a series of gray-colored turbid fractions, marking the void volume, and before the peak of methyl-coenzyme M reductase, identified as a green-colored zone which faded to yellow within several hours after collection. The ACDS elution position is consistent with a 2 MDa complex, and the elution profile is similar to what was found for ACDS from *M. barkeri* in previous work (11). Analytical size exclusion chromatography using a Superose 6 HR column showed a very large complex (also consistent with the expected ~2 MDa size), and most notably the near absence of smaller particles of  $\alpha_2\epsilon_2$  CODH (220 kDa, which elutes at the 26 min position)—see *SI Appendix, Fig. S20*. The high molecular weight ACDS peak exhibited approximately constant CODH-specific activity, and 4 to 7 (usually 5) high-molecular fractions with the highest activity were pooled. A 50-mL Amicon stirred cell with YM30 ultrafiltration membrane was then used at ~10 psi N<sub>2</sub> overpressure to concentrate the ACDS pool to about 8 to 10 mL. Diafiltration was then performed to reduce the salt concentration prior to freezing, by adding 10 mL of H<sub>2</sub>O to the concentrate and reconcentration, which was done twice, ending at a final volume of ~5 mL. The ACDS concentrate was drip-frozen in liquid N<sub>2</sub> and stored in the vapor phase of a liquid N<sub>2</sub> storage system. Addition of ~1,000 U Benzonase nuclease (Sigma) and 1 mM MgCl<sub>2</sub> to the pool prior to concentration resulted in preparations with noticeably lower absorbance at 260 nm. The final A<sub>280</sub>/A<sub>400</sub> ratio was typically in the range of 4.8 to 5.0. Under the assay conditions described, ACDS exhibited a CODH-specific activity of 34.9 ± 2.3 U/mg (n = 6). The preparations also exhibit corrinoid methyltransfer activity using methylcobinamide as a donor and tetrahydrosarcinapterin (H<sub>4</sub>SPT) as acceptor. CO, CO<sub>2</sub>, and CoA exchange activities were characterized previously as well on similarly prepared ACDS sample to confirm full ACDS activity under these preparation conditions.

**Cryogenic Electron Microscopy Grid Preparation.** To prepare blot-plunged cryo-EM samples, an aliquot of purified ACDS was thawed inside of a Coy anaerobic chamber (N<sub>2</sub>/H<sub>2</sub> atmosphere) and diluted to a concentration of 1 mg/mL in 25 mM MOPS and 25 mM Na<sub>2</sub>SO<sub>4</sub>, pH 7.2. The protein sample was supplemented with 0.1% glutaraldehyde. Quantifoil 1.2 μm hole, 1.3 μm spacing Cu 300 mesh holey-carbon grids (EMS) were glow-discharged for 60 s at -15 mA using a PELCO easiGlow system (Ted Pella). Grids were brought into the anaerobic chamber directly after glow discharging. Grids were loaded into the blotting chamber of a Cryoplunge 3 device (Cp3, Gatan), which was maintained at >80% humidity, and allowed to humidify for ~30 s before 3 μL of sample was applied to the carbon-coated side of the grid. The sample was left for ~30 s before blotting for 4 s, with blot settings of -1.0 mm on the sample-facing blotter and -0.5 mm on the back-facing blotter, and plunged in liquid ethane. Grids were transferred to buttons under liquid nitrogen, removed from the anaerobic chamber, and stored under liquid nitrogen.

To prepare chameleon-plunged cryo-EM sample, an aliquot of purified ACDS was thawed inside of a Coy anaerobic chamber and diluted to a concentration of 4 mg/mL in 25 mM MOPS and 25 mM Na<sub>2</sub>SO<sub>4</sub>, pH 7.2. The protein was flash-frozen in liquid nitrogen, transported to the chameleon (SPT Labtech) instrument frozen under liquid nitrogen, thawed, loaded into the chameleon sample vial, and immediately aspirated into the chameleon dispenser. Self-wicking 1.2 μm hole, 0.8 μm spacing holey-carbon grids (SPT Labtech) were glow-discharged for 35 s at -12 mA using the chameleon on-board glow discharger (SPT Labtech). The cryo-EM specimen was frozen using a dispense-to-plunge time of 150 ms (humidity 82%) and stored under liquid nitrogen.

**Cryo-EM Data Collection.** Samples were screened at the Cryo-EM facility in MIT.nano at the Massachusetts Institute of Technology (MIT) on a FEI Talos Arctica G2 Cryo 200 kV transmission electron microscope equipped with a Falcon 3EC camera. All data were collected at the Cryo-EM facility in MIT.nano at MIT on a Titan Krios G3i 300 kV Cryo transmission electron microscope equipped with a K3 Gatan Direct Detector using Thermo Fisher Scientific EPU software. For the specimen that was plunged on the Cryoplunge 3, a dataset was collected at a magnification of 105,000× in superresolution mode and binned by 2 during collection, resulting in a pixel size of 0.832 Å. In total, 14,078 movies were collected with 21 frames, 54.53 e<sup>-</sup>/Å<sup>2</sup> total exposure, and a defocus range of -0.8 to -2.1 μm (*SI Appendix, Table S1*). For the specimen that was plunged on the chameleon, a dataset was collected at a magnification of 130,000× in superresolution mode and binned by 2 during collection, resulting in a pixel size of 0.654 Å. In total, 13,892 movies were collected with 40 frames, 47.1 e<sup>-</sup>/Å<sup>2</sup> total exposure, and a defocus range of 0.0 to -1.75 μm (*SI Appendix, Table S1*).

**Cryo-EM Data Processing.** Cryo-EM data processing was carried out using a combination of cryoSPARC v3.3.2 (65), pyem v0.5 (72), RELION v4.0 (66), and cryoDRGN v0.3.4 (67, 68). For the dataset collected on the Cp3-plunged grid, the data processing workflow is summarized in *SI Appendix*, Fig. S5. For the dataset collected on the chameleon-plunged grid, the data processing workflow is summarized in *SI Appendix*, Figs. S7–S9. See *SI Appendix* for details.

**Model Building and Coordinate Refinement.** A starting model of CODH/ACS hexamer was generated using the COSMIC2 implementation (73) of AlphaFold multimer (74), which gave correct overall shape at low resolution (maps of 5 Å resolution or lower), but upon experimental visualization of secondary structure via EM density, it was evident that the conformation of CODH/ACS differed significantly from the AlphaFold prediction. CODH/ACS AlphaFold prediction was split into components: CODH  $\alpha_2\epsilon_2$ , ACS  $\beta$  residues 1 to 183, ACS  $\beta$  residues 184 to 397. Residues 398 to 472 of ACS  $\beta$  were excluded, as there was no EM density present in any map consistent with this C-terminal region of ACS. CODH  $\alpha_2\epsilon_2$  was docked into all four maps (CODH tetramer Cp3-plunged, CODH tetramer chameleon-plunged, CODH/ACS pentamer, CODH/ACS hexamer) in ChimeraX (75). ACS  $\beta$  components were docked into CODH/ACS pentamer and CODH/ACS hexamer maps in ChimeraX. Each model was subjected to manual refinements in coot (76). Appropriate cofactors (Fe-S and Ni-Fe-S clusters) were added in coot. At the proximal nickel of the A-cluster (in the pentamer and hexamer), extra density was observed consistent with another ligand in addition to the two thiol (Cys278 and Cys280) and one sulfide ligands. Extra density was consistent with a CO ligand, which was modeled in coot. Models were iteratively real-space refined in Phenix (77) using noncrystallographic symmetry (NCS) restraints for the tetramer and hexamer. Custom parameter files were used to restrain the metallocluster geometries during refinement. In final stages of model building, C-terminal density of the  $\beta$  subunit was reexamined and the model was extended by a few residues where possible (*SI Appendix*, Table S1). Some of the software

used was packaged by SBGrid (78). Data collection, refinement, and validation are presented in *SI Appendix*, Table S1.

**Computational Channel Prediction.** Internal channel prediction was performed by MOLEonline (79) using default cavity parameters including a probe radius of 5 Å (upper bound of channel radius) and an interior threshold of 1.1 Å (lower bound of channel radius).

**Data, Materials, and Software Availability.** Coordinates and EM data have been deposited in the protein data bank (PDBID 9COQ (80), 9COR (81), 9COS (82), and 9COT (83)), the electron microscopy data bank (EMDB) (EMD-45089 (84), EMD-45090 (85), EMD-45091 (86), and EMD-45092 (87)) and the electron microscopy public image archive (EMPIAR) EMPIAR-12108 (88) and EMPIAR-12124 (89). All other data are included in the manuscript and/or *SI Appendix*.

**ACKNOWLEDGMENTS.** Specimens were prepared and imaged at the Department of Biology Cryo-EM Facility in MIT.nano with assistance from Dr. Ed Brignole. We thank Dr. Talya S. Levitz for assistance with sample preparation on the chameleon. We thank Dr. Simonida Gencic for expert assistance in purification of the acetyl-CoA decarbonylase/synthase complex. Specimens were screened on a Talos Arctica microscope, which was a gift from the Arnold and Mabel Beckman Foundation. The chameleon was purchased using funds from the HHMI Transformative Technology 2019 Award. This work was supported by NIH Grant R35 GM126982 (to C.L.D.). C.L.D. is a HHMI Investigator.

Author affiliations: <sup>a</sup>Department of Chemistry, Massachusetts Institute of Technology, Cambridge, MA 02139; <sup>b</sup>Department of Biochemistry and Molecular Biology, Uniformed Services University of the Health Sciences, Bethesda, MD 20814; <sup>c</sup>Department of Biology, Massachusetts Institute of Technology, Cambridge, MA 02139; and <sup>d</sup>HHMI, Massachusetts Institute of Technology, Cambridge, MA 02139

1. W. F. Martin, Older than genes: The acetyl CoA pathway and origins. *Front. Microbiol.* **11**, 1–21 (2020).
2. F. L. Sousa, W. F. Martin, Biochemical fossils of the ancient transition from geoenergetics to bioenergetics in prokaryotic one carbon compound metabolism. *Biochim. Biophys. Acta, Bioenerg.* **1837**, 964–981 (2014).
3. S. W. Ragsdale, Enzymology of the Wood-Ljungdahl pathway of acetogenesis. *Ann. N. Y. Acad. Sci.* **1125**, 129–136 (2008).
4. P. S. Adam, G. Borrel, S. Gribaldo, Evolutionary history of carbon monoxide dehydrogenase/acetyl-CoA synthase, one of the oldest enzymatic complexes. *Proc. Natl. Acad. Sci. U.S.A.* **115**, E1166–E1173 (2018).
5. R. K. Thauer, Biochemistry of methanogenesis: A tribute to Marjory Stephenson: 1998 Marjory Stephenson prize lecture. *Microbiology* **144**, 2377–2406 (1998).
6. H. L. Drake, "Acetogenesis, acetogenic bacteria, and the acetyl-CoA "Wood/Ljungdahl" pathway: Past and current perspectives" in *Acetogenesis*, H. L. Drake, Ed. (Springer US, Boston, MA, 1994), pp. 3–60.
7. J. Seravalli, S. W. Ragsdale, Channeling of carbon monoxide during anaerobic carbon dioxide fixation. *Biochemistry* **39**, 1274–1277 (2000).
8. X. Tan, H.-K. Loke, S. Fitch, P. A. Lindahl, The tunnel of acetyl-coenzyme a synthase/carbon monoxide dehydrogenase regulates delivery of CO to the active site. *J. Am. Chem. Soc.* **127**, 5833–5839 (2005).
9. S. I. Hu, E. Pezacka, H. G. Wood, Acetate synthesis from carbon monoxide by *Clostridium thermoaceticum*. Purification of the corrinoid protein. *J. Biol. Chem.* **259**, 8892–8897 (1984).
10. S. W. Ragsdale, J. E. Clark, L. G. Ljungdahl, L. L. Lundie, H. L. Drake, Properties of purified carbon monoxide dehydrogenase from *Clostridium thermoaceticum*, a nickel, iron-sulfur protein. *J. Biol. Chem.* **258**, 2364–2369 (1983).
11. D. A. Grahame, Catalysis of acetyl-CoA cleavage and tetrahydrosarcinapterin methylation by a carbon monoxide dehydrogenase–corrinoid enzyme complex. *J. Biol. Chem.* **266**, 22227–22233 (1991).
12. K. C. Terlesky, M. J. Nelson, J. G. Ferry, Isolation of an enzyme complex with carbon monoxide dehydrogenase activity containing corrinoid and nickel from acetate-grown *Methanosarcina thermophila*. *J. Bacteriol.* **168**, 1053–1058 (1986).
13. D. A. Grahame, D. E. DeMoll, Substrate and accessory protein requirements and thermodynamics of acetyl-CoA synthesis and cleavage in *Methanosarcina barkeri*. *Biochemistry* **34**, 4617–4624 (1995).
14. R. K. Thauer, A. K. Kaster, H. Seedorf, W. Buckel, R. Hedderich, *Methanogenic archaea*: Ecologically relevant differences in energy conservation. *Nat. Rev. Microbiol.* **6**, 579–591 (2008).
15. J. G. Ferry, Methane from acetate. *J. Bacteriol.* **174**, 5489–5495 (1992).
16. K. E. Hammel, K. L. Cornwell, G. B. Diekert, R. K. Thauer, Evidence for a nickel-containing carbon monoxide dehydrogenase in *Methanobrevibacter arboriphilicus*. *J. Bacteriol.* **157**, 975–978 (1984).
17. I. A. Berg *et al.*, Autotrophic carbon fixation in archaea. *Nat. Rev. Microbiol.* **8**, 447–460 (2010).
18. S. A. Ensign, P. W. Ludden, Characterization of the CO oxidation/H<sub>2</sub> evolution system of *Rhodospirillum rubrum*. *J. Biol. Chem.* **266**, 18395–18403 (1991).
19. G. W. Bartholomew, M. Alexander, Microbial metabolism of carbon monoxide in culture and in soil. *Appl. Environ. Microbiol.* **37**, 932–937 (1979).
20. C. L. Drennan, J. Heo, M. D. Sintchak, E. Schreiter, P. W. Ludden, Life on carbon monoxide: X-ray structure of *Rhodospirillum rubrum* Ni-Fe-S carbon monoxide dehydrogenase. *Proc. Natl. Acad. Sci. U.S.A.* **98**, 11973–11978 (2001).
21. H. Dobbek, V. Svetlichnyi, L. Gremec, R. Huber, O. Meyer, Crystal structure of a carbon monoxide dehydrogenase reveals a [Ni–4Fe–5S] cluster. *Science* **293**, 1281–1285 (2001).
22. H. Dobbek, V. Svetlichnyi, J. Liss, O. Meyer, Carbon monoxide induced decomposition of the active site [Ni–4Fe–5S] cluster of CO dehydrogenase. *J. Am. Chem. Soc.* **126**, 5382–5387 (2004).
23. L. Dominik *et al.*, CODH-IV: A high-efficiency CO-scavenging CO dehydrogenase with resistance to O<sub>2</sub>. *Angew. Chem. Int. Ed.* **56**, 15466–15469 (2017).
24. E. C. Wittenborn *et al.*, Redox-dependent rearrangements of the NiFeS cluster of carbon monoxide dehydrogenase. *eLife* **7**, e39451 (2018).
25. T. I. Doukov, T. M. Iverson, J. Seravalli, S. W. Ragsdale, C. L. Drennan, A Ni–Fe–Cu center in a bifunctional carbon monoxide dehydrogenase/acetyl-CoA synthase. *Science* **298**, 567–572 (2002).
26. O. N. Lemaire, T. Wagner, Gas channel rerouting in a primordial enzyme: Structural insights of the carbon-monoxide dehydrogenase/acetyl-CoA synthase complex from the acetogen *Clostridium autoethanogenum*. *Biochim. Biophys. Acta, Bioenerg.* **1862**, 148330 (2021).
27. E. Kocsis, M. Kessel, E. DeMoll, D. A. Grahame, Structure of the Ni/Fe-S protein subcomponent of the acetyl-CoA decarbonylase/synthase complex from *Methanosarcina thermophila* at 26-Å resolution. *J. Struct. Biol.* **128**, 165–174 (1999).
28. W. Gong *et al.*, Structure of the  $\alpha_2\epsilon_2$  Ni-dependent CO dehydrogenase component of the *Methanosarcina barkeri* acetyl-CoA decarbonylase/synthase complex. *Proc. Natl. Acad. Sci. U.S.A.* **105**, 9558–9563 (2008).
29. S. E. Cohen *et al.*, Crystallographic characterization of the carbonylated A-cluster in carbon monoxide dehydrogenase/acetyl-CoA synthase. *ACS Catal.* **10**, 9741–9746 (2020).
30. C. D. James, S. Wiley, S. W. Ragsdale, B. M. Hoffman, <sup>13</sup>C electron nuclear double resonance spectroscopy shows acetyl-CoA synthase binds two substrate CO in multiple binding modes and reveals the importance of a CO-binding "Alcove". *J. Am. Chem. Soc.* **142**, 15362–15370 (2020).
31. C. Darnault *et al.*, Ni-Zn-[Fe4–S4] and Ni-Ni-[Fe4–S4] clusters in closed and open  $\alpha$  subunits of acetyl-CoA synthase/carbon monoxide dehydrogenase. *Nat. Struct. Mol. Biol.* **10**, 271–279 (2003).
32. S. E. Cohen *et al.*, Negative-stain electron microscopy reveals dramatic structural rearrangements in Ni-Fe-S-dependent carbon monoxide dehydrogenase/acetyl-CoA synthase. *Structure* **29**, 43–49 (2020).
33. D. A. Grahame, E. DeMoll, Partial reactions catalyzed by protein components of the acetyl-CoA decarbonylase synthase enzyme complex from *Methanosarcina barkeri*. *J. Biol. Chem.* **271**, 8352–8358 (1996).
34. E. Murakami, S. W. Ragsdale, Evidence for intersubunit communication during acetyl-CoA cleavage by the multienzyme CO dehydrogenase/acetyl-CoA synthase complex from *Methanosarcina thermophila*. Evidence that the beta subunit catalyzes C-C and C-S bond cleavage. *J. Biol. Chem.* **275**, 4699–4707 (2000).
35. J. A. Krzycki, L. E. Mortenson, R. C. Prince, Paramagnetic centers of carbon monoxide dehydrogenase from aceticlastic *Methanosarcina barkeri*. *J. Biol. Chem.* **264**, 7217–7221 (1989).
36. M. C. Darrow, J. P. Moore, R. J. Walker, K. Doering, R. S. King, Chameleon: Next generation sample preparation for CryoEM based on spotiton. *Microsc. Microanal.* **25**, 994–995 (2019).
37. H. Wei *et al.*, Spotiton and chameleon vitrification robots. *Microsc. Microanal.* **25**, 1010–1011 (2019).
38. I. Razinkov *et al.*, A new method for vitrifying samples for cryoEM. *J. Struct. Biol.* **195**, 190–198 (2016).
39. V. P. Danedy *et al.*, Spotiton: New features and applications. *J. Struct. Biol.* **202**, 161–169 (2018).

40. T. S. Levitz *et al.*, Approaches to using the chameleon: Robust, automated, fast-plunge cryoEM specimen preparation. *Front. Mol. Biosci.* **9**, 1–10 (2022).
41. T. S. Levitz, E. J. Brignole, I. Fong, M. C. Darrow, C. L. Drennan, Effects of chameleon dispense-to-plunge speed on particle concentration, complex formation, and final resolution: A case study using the *Neisseria gonorrhoeae* ribonucleotide reductase inactive complex. *J. Struct. Biol.* **214**, 1–25 (2022).
42. S. Vasquez *et al.*, Structural and biochemical investigations of a HEAT-repeat protein involved in the cytosolic iron-sulfur cluster assembly pathway. *Commun. Biol.* **6**, 1–12 (2023).
43. S. Gencic, K. Kelly, S. Ghebreamlak, E. C. Duin, D. A. Grahame, Different modes of carbon monoxide binding to acetyl-CoA synthase and the role of a conserved phenylalanine in the coordination environment of nickel. *Biochemistry* **52**, 1705–1716 (2013).
44. A. Voldeda, C. Darnault, X. Tan, P. A. Lindahl, J. C. Fontecilla-Camps, Novel domain arrangement in the crystal structure of a truncated acetyl-CoA synthase from *Moorella thermoacetica*. *Biochemistry* **48**, 7916–7926 (2009).
45. A. Biester, S. Dementin, C. L. Drennan, Visualizing the gas channel of a monofunctional carbon monoxide dehydrogenase. *J. Inorg. Biochem.* **230**, 1–11 (2022).
46. T. I. Doukov, L. C. Blasiak, J. Seravalli, S. W. Ragsdale, C. L. Drennan, Xenon in and at the end of the tunnel of bifunctional carbon monoxide dehydrogenase/acetyl-CoA synthase. *Biochemistry* **47**, 3474–3483 (2008).
47. S. Gencic, E. C. Duin, D. A. Grahame, Tight coupling of partial reactions in the acetyl-CoA decarbonylase/synthase (ACDS) multienzyme complex from *Methanoscincus thermophila*: Acetyl C-C bond fragmentation at the A-cluster promoted by protein conformational changes. *J. Biol. Chem.* **285**, 15450–15463 (2010).
48. M. Hügler, S. M. Sievert, Beyond the calvin cycle: Autotrophic carbon fixation in the ocean. *Annu. Rev. Mar. Sci.* **3**, 261–289 (2011).
49. I. Sánchez-Andrea *et al.*, The additive glycine pathway allows autotrophic growth of *Desulfovibrio desulfuricans*. *Nat. Commun.* **11**, 5090 (2020).
50. L. Wu, R. Wang, Carbon monoxide: Endogenous production, physiological functions, and pharmacological applications. *Pharmacol. Rev.* **57**, 585–630 (2005).
51. T. L. Miller, M. J. Wolin, Methanogens in human and animal intestinal tracts. *Syst. Appl. Microbiol.* **7**, 223–229 (1986).
52. Z. Li *et al.*, Comparative microbiome analysis reveals the ecological relationships between rumen methanogens, acetogens, and their hosts. *Front. Microbiol.* **11**, 1311 (2020).
53. M. Cai *et al.*, Characterization of methyl- and acetyl-Ni intermediates in acetyl CoA synthase formed during anaerobic CO<sub>2</sub> and CO fixation. *J. Am. Chem. Soc.* **145**, 13696–13708 (2023).
54. V. Svetlichnyi *et al.*, A functional Ni-Ni-[4Fe-4S] cluster in the monomeric acetyl-CoA synthase from *Carboxydotothermus hydrogenoformans*. *Proc. Natl. Acad. Sci. U.S.A.* **101**, 446–451 (2004).
55. Y. Kung, T. I. Doukov, J. Seravalli, S. W. Ragsdale, C. L. Drennan, Crystallographic snapshots of cyanide- and water-bound C-clusters from bifunctional carbon monoxide dehydrogenase/acetyl-CoA synthase. *Biochemistry* **48**, 7432–7440 (2009).
56. J. Ruickoldt, Y. Basak, L. Domnik, J.-H. Jeoung, H. Dobbek, On the kinetics of CO<sub>2</sub> reduction by Ni, Fe-Co dehydrogenases. *ACS Catal.* **12**, 13131–13142 (2022).
57. E. Krissinel, K. Henrik, Inference of macromolecular assemblies from crystalline state. *J. Mol. Biol.* **372**, 774–797 (2007).
58. S. Menon, S. W. Ragsdale, Role of the [4Fe-4S] cluster in reductive activation of the cobalt center of the corrinoid iron-sulfur protein from *Clostridium thermoaceticum* during acetate biosynthesis. *Biochemistry* **37**, 5689–5698 (1998).
59. S. Menon, S. W. Ragsdale, The role of an iron-sulfur cluster in an enzymatic methylation reaction: Methylation of CO dehydrogenase/acetyl-CoA synthase by the methylated corrinoid iron-sulfur protein. *J. Biol. Chem.* **274**, 11513–11518 (1999).
60. S. W. Ragsdale, "Biological carbon fixation by an organometallic pathway: Evidence supporting the paramagnetic mechanism of the nickel-iron-sulfur acetyl-CoA synthase" in *Comprehensive Coordination Chemistry III*, E. C. Constable, G. Parkin, L. Que, Eds. (Elsevier, Oxford, UK, 2021), pp. 611–633.
61. J. Seravalli, S. W. Ragsdale, Pulse-chase studies of the synthesis of acetyl-CoA by carbon monoxide dehydrogenase/acetyl-CoA synthase: Evidence for a random mechanism of methyl and carbonyl addition. *J. Biol. Chem.* **283**, 8384–8394 (2008).
62. D. P. Barondeau, P. A. Lindahl, Methylation of carbon monoxide dehydrogenase from *Clostridium thermoaceticum* and mechanism of acetyl coenzyme A synthesis. *J. Am. Chem. Soc.* **119**, 3959–3970 (1997).
63. P. A. Lindahl, E. Münck, S. W. Ragsdale, CO dehydrogenase from *Clostridium thermoaceticum*. EPR and electrochemical studies in CO<sub>2</sub> and argon atmospheres. *J. Biol. Chem.* **265**, 3873–3879 (1990).
64. W. Kühlbrandt, The resolution revolution. *Science* **343**, 1443–1444 (2014).
65. A. Punjani, J. L. Rubinstein, D. J. Fleet, M. A. Brubaker, cryoSPARC: Algorithms for rapid unsupervised cryo-EM structure determination. *Nat. Methods* **14**, 290–296 (2017).
66. D. Kimanis, L. Dong, G. Sharov, T. Nakane, S. H. W. Scheres, New tools for automated cryo-EM single-particle analysis in RELION-4.0. *Biochem. J.* **478**, 4169–4185 (2021).
67. L. F. Kinman, B. M. Powell, E. D. Zhong, B. Berger, J. H. Davis, Uncovering structural ensembles from single-particle cryo-EM data using cryoDRGN. *Nat. Protoc.* **18**, 319–339 (2023).
68. E. D. Zhong, T. Bepler, B. Berger, J. H. Davis, CryoDRGN: Reconstruction of heterogeneous cryo-EM structures using neural networks. *Nat. Methods* **18**, 176–185 (2021).
69. D. A. Grahame, T. C. Stadtman, Carbon monoxide dehydrogenase from *Methanoscincus barkeri*. Disaggregation, purification, and physicochemical properties of the enzyme. *J. Biol. Chem.* **262**, 3706–3712 (1987).
70. S. E. Cohen, *Multienzyme Assemblies and Dynamics in Acetogenesis and Methanogenesis* (Massachusetts Institute of Technology, DSpace@MIT, 2020).
71. M. M. Bradford, A rapid and sensitive method for the quantitation of microgram quantities of protein utilizing the principle of protein-dye binding. *Anal. Biochem.* **72**, 248–254 (1976).
72. D. Asarnow, E. Palovcak, Y. Cheng, UCSF pyem v0.5, Zenodo (2019). <https://doi.org/10.5281/zenodo.3576630>. Accessed 16 December 2019.
73. M. A. Cianfrrocco, M. Wong-Barnum, C. Youn, R. Wagner, A. Leschziner, "COSMIC2: A science gateway for cryo-electron microscopy structure determination" in *Proceedings of the Practice and Experience in Advanced Research Computing 2017 on Sustainability, Success and Impact* (Association for Computing Machinery, New Orleans, LA, 2017), p. 22.
74. R. Evans *et al.*, Protein complex prediction with AlphaFold-Multimer. *bioRxiv* [Preprint] (2022). <https://doi.org/10.1101/2021.10.04.463034> (Accessed 3 August 2023).
75. E. F. Pettersen *et al.*, UCSF ChimeraX: Structure visualization for researchers, educators, and developers. *Protein Sci.* **30**, 70–82 (2021).
76. P. Emsley, B. Lohkamp, W. G. Scott, K. Cowtan, Features and development of Coot. *Acta Crystallogr. D, Biol. Crystallogr.* **66**, 486–501 (2010).
77. D. Liebschner *et al.*, Macromolecular structure determination using X-rays, neutrons and electrons: Recent developments in Phenix. *Acta Crystallogr. D, Biol. Crystallogr.* **75**, 861–877 (2019).
78. A. Morin *et al.*, Collaboration gets the most out of software. *eLife* **2**, e01456 (2013).
79. L. Pravda *et al.*, MOLEonline: A web-based tool for analyzing channels, tunnels and pores (2018 update). *Nucleic Acids Res.* **46**, W368–W373 (2018).
80. A. Biester, C. L. Drennan, Carbon monoxide dehydrogenase (CODH) from *Methanoscincus thermophila*, specimen prepared on blot plunger. Worldwide Protein Data Bank (wwPDB). <http://doi.org/10.2210/pdb9C0/pdb>. Deposited 27 May 2024.
81. A. Biester, C. L. Drennan, Carbon monoxide dehydrogenase (CODH) from *Methanoscincus thermophila*, specimen prepared on chameleon plunger. Worldwide Protein Data Bank (wwPDB). <http://doi.org/10.2210/pdb9C0/pdb>. Deposited 27 May 2024.
82. A. Biester, C. L. Drennan, Carbon monoxide dehydrogenase/acetyl-CoA synthase (CODH/ACS) pentamer from *Methanoscincus thermophila*. Worldwide Protein Data Bank (wwPDB). <http://doi.org/10.2210/pdb9C0/pdb>. Deposited 27 May 2024.
83. A. Biester, C. L. Drennan, Carbon monoxide dehydrogenase/acetyl-CoA synthase (CODH/ACS) hexamer from *Methanoscincus thermophila*. Worldwide Protein Data Bank (wwPDB). <http://doi.org/10.2210/pdb9C0/pdb>. Deposited 27 May 2024.
84. A. Biester, C. L. Drennan, Carbon monoxide dehydrogenase (CODH) from *Methanoscincus thermophila*, specimen prepared on blot plunger. Electron Microscopy Data Bank (EMDB). <https://www.ebi.ac.uk/emdb/EMD-45089>. Deposited 27 May 2024.
85. A. Biester, C. L. Drennan, Carbon monoxide dehydrogenase (CODH) from *Methanoscincus thermophila*, specimen prepared on chameleon plunger. Electron Microscopy Data Bank (EMDB). <https://www.ebi.ac.uk/emdb/EMD-45090>. Deposited 27 May 2024.
86. A. Biester, C. L. Drennan, Carbon monoxide dehydrogenase/acetyl-CoA synthase (CODH/ACS) pentamer from *Methanoscincus thermophila*. Electron Microscopy Data Bank (EMDB). <https://www.ebi.ac.uk/emdb/EMD-45091>. Deposited 27 May 2024.
87. A. Biester, C. L. Drennan, Carbon monoxide dehydrogenase/acetyl-CoA synthase (CODH/ACS) hexamer from *Methanoscincus thermophila*. Electron Microscopy Data Bank (EMDB). <https://www.ebi.ac.uk/emdb/EMD-45092>. Deposited 27 May 2024.
88. A. Biester, C. L. Drennan, Cryogenic electron microscopy of blot-plunged acetyl-CoA decarbonylase synthase. Electron Microscopy Public Image Archive (EMPIAR). <https://www.ebi.ac.uk/empiar/EMPIAR-12108>. Deposited 31 May 2024.
89. A. Biester, C. L. Drennan, Cryogenic electron microscopy of chameleon-plunged acetyl-CoA decarbonylase/synthase. Electron Microscopy Public Image Archive (EMPIAR). <https://www.ebi.ac.uk/empiar/EMPIAR-12124>. Deposited 10 June 2024.